ACS APPLIED MATERIALS & INTERFACES

www.acsami.org Research Article

3D Printing of Polyethylene Terephthalate Glycol–Sepiolite Composites with Nanoscale Orientation

Hoon Kim, Kwang-Hyun Ryu, Dooyoung Baek, Tanveer Ahmed Khan, Hyun-Joong Kim,*
Sungchul Shin, Jinho Hyun, Jin Soo Ahn, Sug-Joon Ahn, Hyun Jeong Kim, and Jaseung Koo

Cite This: *ACS Appl. Mater. Interfaces* 2020, 12, 23453–23463 Read Online

ACCESS | Metrics & More | Article Recommendations | SI Supporting Information

ABSTRACT: A fused-deposition modeling (FDM) 3D-printed polyethylene terephthalate glycol (PETG)–sepiolite composite showed effective synergetic mechanical reinforcement in tensile testing compared to an injection-molded composite. The results showed that the addition of 3 phr sepiolite improved the tensile strength of 3D-printed PETG samples by 35.4%, while the tensile strength of injection-molded PETG samples was improved by 7.2%. To confirm these phenomena, FDM PETG–sepiolite composites were investigated by small-angle X-ray scattering to correlate the nanostructures of the composites with their mechanical strengths. The small-angle X-ray scattering data and transmission electron microscopy observations demonstrated that needle-shaped sepiolite particles were aligned in the printing direction. This fine oriented nanostructure formed during 3D printing created a synergistic effect that improved the material properties of the composite. These novel PETG–sepiolite composites with enhanced mechanical properties can be promising materials fabricated via FDM 3D printing.

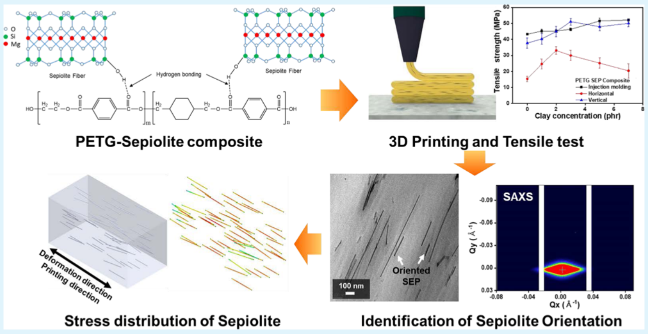

KEYWORDS: *3D printing, polyethylene terephthalate glycol, nanoclay, nanocomposite, mechanical strength, small-angle X-ray scattering*

1. INTRODUCTION

Polymer nanocomposite technologies are widely utilized to fabricate 3D objects for diverse applications. The fused deposition modeling (FDM) method of melting polymers for 3D printing has been widely studied in industrial and research fields because it permits the use of various types of thermoplastic polymers.[1−3] The selection of polymers is very important because the material properties of the thermoplastic polymers applied in FDM are closely related to the completeness of printing and the physical properties of the 3D-printed object.[4] Many thermoplastic polymers, including polypropylene, acrylonitrile butadiene styrene, polylactic acid, polyethylene terephthalate, polyethylene terephthalate glycol (PETG), nylon, and polyurethane-based thermoplastics, are used for FDM 3D printing.[2−11] Among these, amorphous PETG is widely used because it features good impact and tear strengths, barrier properties, chemical resistance, and transparency. Therefore, it is suitable for 3D printing and requires additional research.[7,12,13] However, because of the limitations of the FDM 3D printing method, printed PETG exhibits poorer physical properties than injection-molded PETG because of the weak points between layers.[14]

To overcome this limitation of the FDM 3D printing method, polymer composite technology can be applied.[2−6] However, the application of composite materials to 3D printing entails some problems. The most important issue is the size of the additive used in the composite material. As the size of the additive increases, the size of the printer nozzle must also increase, which decreases the printing resolution.[5,15] Therefore, nanomaterials must be used as filler to achieve high resolution. However, nanomaterials such as graphene and carbon nanotubes (CNTs) are disadvantageous for widespread use, as they are high in price. Nanoclays have reasonable prices and are therefore more suitable for industrial application.[16] Several clays have been used as reinforcing filler—among these is sepiolite (SEP), a hydrated magnesium silicate with the half-unit-cell formula of $Mg_8Si_{12}O_{30}(OH)_4 \cdot 12H_2O$. It has a needle-like or fiber-like morphology comprising several blocks and tunnels oriented parallel to the fiber direction. Each structural block contains a central octahedral magnesium ($MgOH_6$) sheet sandwiched by two tetrahedral silica (SiO_4) sheets. A single SEP fiber has dimensions of 0.2–4 μm in length, 10–30 nm in width, and 5–10 nm in thickness.[17,18]

Polymer–SEP composites have recently attracted attention because of the high aspect ratio of SEP fibers and the good

Received: February 28, 2020
Accepted: April 30, 2020
Published: April 30, 2020

https://dx.doi.org/10.1021/acsami.0c03830
ACS Appl. Mater. Interfaces 2020, 12, 23453−23463

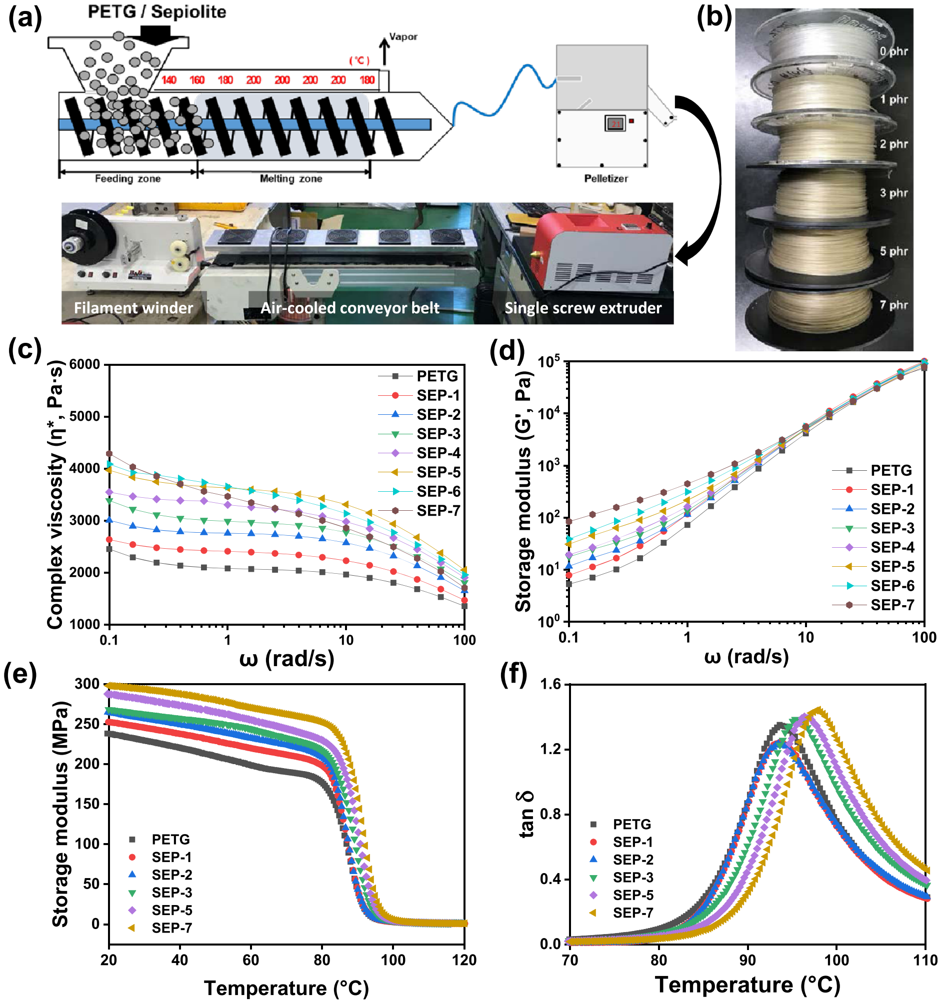

Figure 1. The process of manufacturing PETG and PETG−SEP composite filaments and the rheological characterization of the materials. (a) Schematic of preparation of FDM 3D printer filament. (b) PETG and PETG−SEP filament for 3D printers with SEP concentrations of 1−7 phr. The curves of (c) complex viscosity η^* and (d) storage modulus G' with frequency ω for the pure PETG and PETG−SEP nanocomposites in molten state at 200 °C. Temperature dependencies of (e) storage modulus G' and (f) tan δ (ratio of loss modulus to storage modulus) of pure PETG and PETG−SEP nanocomposites.

thermomechanical properties of the composites. With strong interfacial bonding forces between the filler and the polymer resin, a homogeneous dispersion state can be achieved. This improves the thermal and mechanical properties and introduces flame-retardancy in the composite material.[18,19] In this study, composites were fabricated using PETG and SEP and applied in 3D printing. The 3D-printed composites showed higher strength than composites formed by conventional injection molding. The FDM 3D-printed PETG−SEP composites showed higher increase rates in physical strength than the injection-molded composites with increasing SEP content.

Several factors affect the properties of 3D printed objects. For example, the printing speed and material temperature are important factors in the 3D printing process.[20] In addition, the rheological behavior of the polymer resin passing through the 3D printer nozzle at high temperature, the diffusion of the polymer chain,[21] the interfacial adhesion factor between resin and filler,[22] and the process−structure−property relationships all affect the bonding strengths of 3D-printed materials.[23] These complex interactions determine the final properties of the material. When using nanomaterial filler, the structure and orientation of the nanomaterial are important factors in 3D printing process.[15,24,25] Therefore, it is necessary to study the orientation and structure of the additives used in composites.

In order to clarify the reason for the synergistic increase in strength shown by the 3D-printed PETG−SEP composites, the rheological, thermomechanical, mechanical, and morphological properties, as well as the nanomaterial orientations and material structures, were measured by viscometry, dynamic mechanical analysis (DMA), universal testing machine (UTM) analysis, transmission electron microscopy (TEM), scanning electron microscopy (SEM), and small-angle X-ray scattering (SAXS). Based on the experimental results, we aim to identify the behavior and orientation of the SEP nanoclay in the PETG polymer during the 3D printing process and to characterize the synergistic effects on the properties of the 3D-printed PETG−SEP composite.

2. MATERIALS AND METHODS

2.1. Materials. SEP was purchased from Sigma-Aldrich (USA), with the structure unit $Mg_2H_2Si_3O_9 \cdot xH_2O$, a diameter of 10−30 nm, and a length of 1−2 μm. For the matrix polymer, PETG or poly(ethylene glycol-*co*-1,4-cyclohexanedimethanol terephthalate) was obtained as PN200 from SK Chemicals (Republic of Korea),

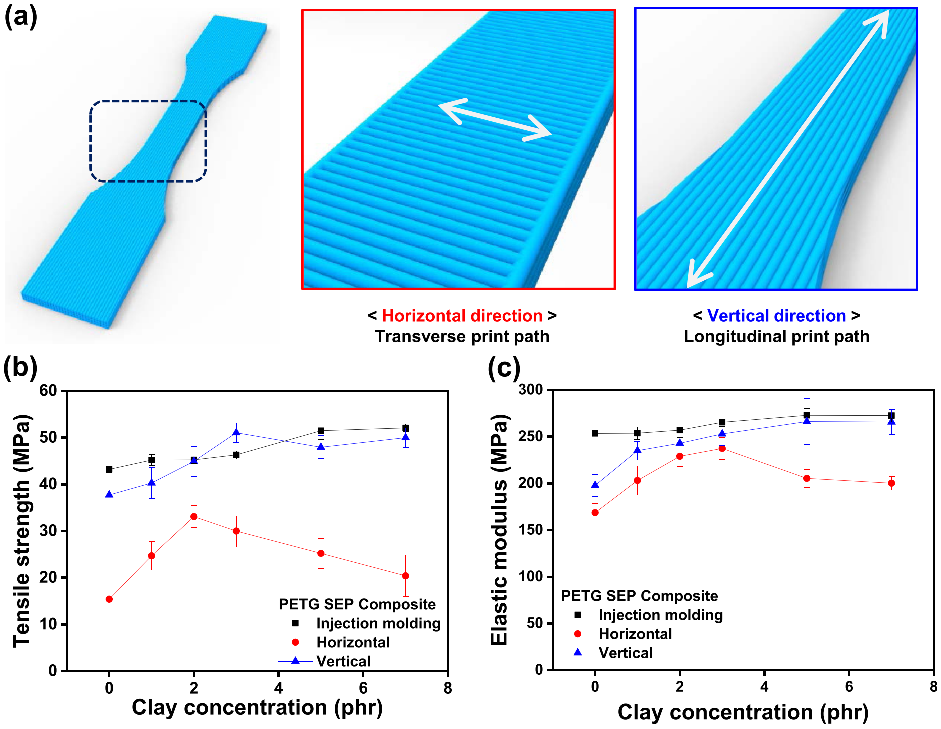

Figure 2. Change of tensile strength characteristics according to 3D printing direction. (a) FDM 3D printer printing direction scheme drawn using Repetier-Host software ver. 2.1.3.; mechanical property measurements: (b) tensile strength and (c) Young's modulus of PETG nanocomposites with varying SEP concentrations.

with a density of 1.27 g/cm^3, a heat distortion temperature of 70 °C at 0.45 MPa, and a glass transition temperature T_g of 80 °C. For TEM sampling, Spurr resin comprising 3,4-epoxycyclohexylmethyl, poly(propylene glycol) diglycidyl ether, nonenyl succinic anhydride, and 2-dimethylaminoethanol (Ted Pella, Inc., Sweden) was selected.

2.2. Preparation of PETG–SEP Nanocomposites. Before the extrusion process, PETG and SEP were each dried in a vacuum oven at 65 °C for about 12 h. The fully dried PETG was physically mixed using a tumbler mixer with different amounts of SEP powder. The composites formed using 1, 2, 3, 5, and 7 parts SEP per hundred resin (phr) of PETG pellets were denoted as SEP-1, SEP-2, SEP-3, SEP-5, and SEP-7, respectively.

PETG and SEP were mixed using a twin-screw extruder (BA-19, Bau Technology, Republic of Korea). After mixing, the composites were cooled by passing through a water bath before pelletization with a pelletizer (Bau Technology, Republic of Korea). The mixing zone of the twin-screw extruder was divided into eight heating zones at temperatures of 140, 160, 180, 200, 200, 200, 200, and 180 °C from the funnel to the extrusion head; the screw speed was 200 rpm. The composite pellets were dried in a vacuum oven at 65 °C for about 12 h and stored to avoid exposure to moisture.

2.3. Preparation of Filaments for FDM 3D Printing. After drying, the pellets of PETG–SEP nanocomposites were discharged into a single-screw extruder (Mini Filament Extrusion Machine FILIBOT H303, Forden Tech Co., Ltd., Republic of Korea). The temperature of the heating zone and extrusion head was 210 °C, while the diameter of the die and the screw speed were 2 mm and 10 rpm, respectively. The filament-making system and the filament for 3D printing are shown in Figure 1a,b. By regulating the rotating speed of the winder (Auto Filament Winder, Bau Technology, Republic of Korea), SEP-reinforced nanocomposite filaments with diameters of 1.75 ± 0.1 mm were obtained. To determine the influence on the properties caused by extrusion, pure PETG filaments were also reproduced by both twin-screw and single-screw extrusion.

2.4. Preparation of Specimens. Samples for mechanical studies of the 3D-printed samples, including tensile strength testing and SAXS analysis, were designed according to ASTM D638-5 and the SAXS solid-sample jig size of 25 × 25 × 1 mm and fabricated with an FDM 3D printer (AEP2, Rokit, Republic of Korea) according to test requirements. As shown in Figure 2a, the tensile strength testing specimens are divided into vertical-direction samples, in which the printing direction is parallel to the deformation direction and horizontal-direction samples and in which the printing direction is perpendicular to the direction of deformation.

All specimens were printed directly on imide film-covered heating plates without supports. The filling rate of the specimens was set to 100%, meaning that all specimens were solid structures. For the tensile testing samples, the total number of printed layers was 16 and the thickness of each layer was set to 200 μm in the program. The temperature of the printer head and the printing speed were set to 250 °C and 60 mm/s, respectively. The temperature of the printing bed was set to 100 °C for stable deposition of the printing material.

Furthermore, tensile samples and DMA specimens were fabricated using an injection molder (Bau Technology, Republic of Korea) to compare the difference between injection molding and 3D printing. The temperature of the injection-molding furnace was 200 °C.

2.5. Characterizations. The tensile strengths of the composite samples were measured using a UTM (AllroundLine Z010, 2 kN load cell, Zwick, Germany) to confirm the changes in material properties and 3D printing effects with increasing SEP content. A crosshead speed of 5 mm/min was used during the measurements, and the mechanical properties were analyzed at room temperature (RT, ~20 °C). Seven specimens of each composition were measured to calculate the margin of error.

In order to confirm the orientations of the needle-shaped SEP particles in the PETG composites after the 3D printing process, the microstructures of the materials were analyzed using SAXS. A schematic of the SAXS measurement is shown in Figure 7a. The FDM 3D-printed material of 1 mm in thickness was rotated by 90° and measured. An X-ray scattering spectrometer (XEUSS 2.0, Xenocs, France) was used for the experiment. The distance between the sample and the detector was 2500 mm and the irradiation time was 600 s. Cu Kα radiation (l = 1.54056 Å) was used with the diffractometer operating at 50 kV and 0.6 mA. All SAXS measurements were performed at RT.

In order to define the degree of orientation of SEP in the 3D-printed PETG−SEP nanocomposites from a morphological perspective, composite specimens were observed using TEM (JEM-2100F, JEOL Co., Japan). The TEM samples were prepared for slicing using Spurr resin.[26]

In order to obtain TEM samples, the 3D-printed composite samples were impregnated by Spurr resin,[26] held for 24 h in vacuum conditions (−0.95 bar) and cured in an oven at 70 °C for 24 h. The cured cone calorimeter residue sample was sliced using an ultramicrotome (EM UC7, Leica, Germany). The sample was boarded on a copper grid and a carbon coating was applied for 30 s to prevent electron charge damage.

In order to confirm the effect of SEP inclusion on the fracture behavior of the polymer composite, the post-tensile-testing fracture surfaces of the 3D-printed samples were observed with field-emission SEM (FE-SEM, SUPRA 55VP, Carl Zeiss, Germany) performed at an acceleration voltage of 10 kV. Before the FE-SEM measurement, each sample was pre-coated with a homogeneous platinum layer (99.99% purity) by ion sputtering to eliminate electron charging.

In the FDM 3D printing process, the molten polymer passes through a nozzle with a diameter of 400 μm. It is necessary to determine the rheological properties of the molten material in order to understand the behavior of the material in passing through the nozzle. For characterization, the molten composites were measured using a rheometer (MCR 302, Anton Paar Ltd., Austria). The diameter of the disposable parallel plate was 25 mm, the experimental temperature was 200 °C, the plate gap was set at 300 μm, and the shear rate was 0.1−100 rad/s.

To indirectly measure the material thermal dynamics and the interfacial bonding of PETG and SEP in the composites, DMA (Q800, TA Instrument, USA) was performed for thermomechanical analysis between 40 and 120 °C with a frequency of 1 Hz and the strain rate of 0.1% using the three-point bending method.

Simulations for PETG−SEP nanocomposite structural analyses were performed using SOLIDWORKS Simulation software by Dassault Systèmes SolidWorks Corporation. The purpose of the structural analysis was to verify the actual experimental results through analysis and to identify their tendencies. The input characteristics of SEP used in the analysis were the elastic modulus and density of 10.58 GPa and 2380 kg/m^3, respectively; for PETG, the elastic modulus and density were 2.05 GPa and 1270 kg/m^3, respectively.

3. RESULTS AND DISCUSSION

3.1. Rheological Properties of PETG−SEP Composite Filaments.

To understand the state of the PETG−SEP composite filament as it passes through the nozzle during 3D printing, determining the rheological properties of the molten polymeric material is necessary. The rheological behavior affects the processability and the structure−processing relationship of the material. Linear dynamic viscoelastic master curves for pure PETG and varying PETG−SEP composites are shown in Figure 1c,d. All samples exhibit stable rheological properties in time-sweep experiments over 20 min. Figure 1c,d presents the complex viscosity η^* and the storage modulus G' versus the frequency ω of the neat PETG and PETG−SEP composites with SEP load varying from 1 to 7 phr.

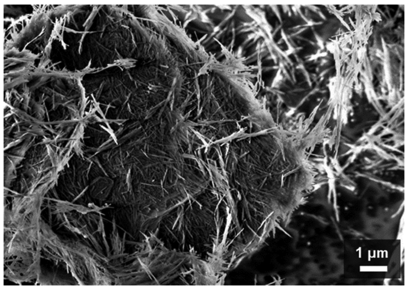

Figure 3. SEM image of the pure SEP powder.

Under vibrational shear, η^* is the ratio of the shear stress amplitude to the strain rate amplitude. A viscoelastic fluid shows a phase lag in its stress and strain responses, and the viscosity can be expressed as real and imaginary parts.[30] G' relates to the imaginary part of the complex viscosity and measures the energy stored in the material for half a vibrational period.

The complex viscosity η^* of pure PETG shows shear-thinning behavior at high ω (Figure 1c) and a long plateau of the storage modulus G' versus ω (Figure 1d). For all nanocomposites, SEP concentrations of ≥ 1 phr affect the rheological properties of PETG. At 7 phr SEP, η^* and G' show approximately two-fold increases over those of pure PETG (Figure 1c,d). All PETG−SEP composite samples exhibit shear-thinning behaviors for η^* with plateau regions at intermediate ω and G' plateaus at low ω. As can be seen in many polymer nanocomposites, because of the good dispersion of SEP in PETG, these results can be attributed to network formation and the transition from liquid- to solid-like behavior.

Similar rheological behaviors under low-amplitude vibrational shear have been reported for other polymer nanocomposites containing clay, cellulose nanocrystals (CNCs), or CNTs with good dispersion.[31−34] Notably, the data for SEP-7 have lower amplitude than that for SEP-5. This can be explained by the more significant aggregate formation at higher SEP contents.

The SEP-7 and SEP-6 viscosity behaviors differ from those of pure PETG and SEP-1, SEP-2, SEP-3, SEP-4, and SEP-5. The complex viscosity η^* of SEP-7 and SEP-6 shows slight shear-thinning behaviors and very steep slopes. A behavioral variation as a precursor to this phenomenon is observed in SEP-6. For composites with SEP contents exceeding the critical point of 6 phr, a sudden phase change occurs. Pure PETG and samples from SEP-1 to SEP-5 demonstrate constant increases in the complex viscosity η * with increasing SEP content. They show the same change in storage modulus; this property relates to the dispersion and entanglement of nanomaterials. Figure S2 schematically depicts the rheological change of the composite material with increasing SEP content; it is similar to that of conventional single-walled CNT−poly(methyl methacrylate) nanocomposites.[35] As shown in Figure S2, for SEP contents exceeding the critical point, nanomaterial entanglement occurs and the rheological properties are rapidly changed with increasing frequency. The most dramatic instances of these phenomena occur in SEP-6 and SEP-7.

DMA was performed to measure the storage moduli of the PETG and the fabricated nanocomposites. The storage modulus curves of the pure PETG and PETG−SEP nanocomposites are shown in Figure 1e,f. By the inclusion of the well-dispersed SEP, a significant increase in the storage modulus is achieved with increases in SEP loading. At 25 °C, the storage modulus of pure PETG is 233.8 MPa; as the SEP content is increased, the storage modulus of the composite tends to increase gradually. For SEP-7, the storage modulus is 295.8 MPa. The tan δ values, which indicate the ratio of the loss moduli to the storage moduli, of the pure

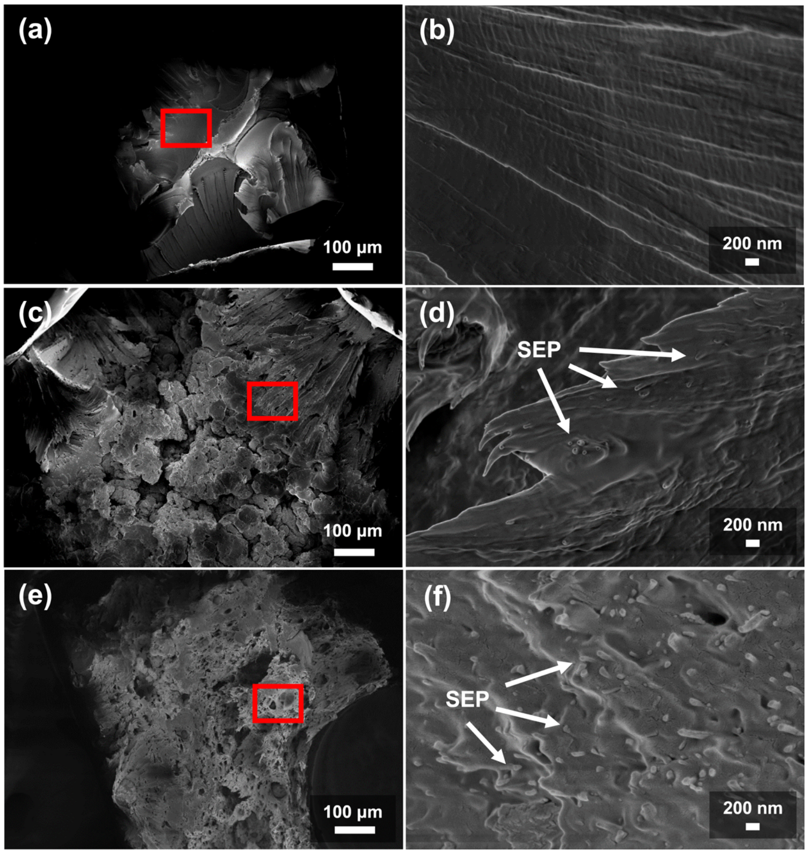

Figure 4. SEM image of post-tensile fracture surface observation of injection-molded PETG composites with tension applied. (a,b) Pure PETG, (c,d) SEP-3 composite, (e,f) SEP-7 composite.

PETG and PETG−SEP nanocomposites are shown in Figure 1f. The maximum tan δ value of pure PETG is observed at 93.5 °C; it is increased with increasing SEP content and observed at 97.9 °C for SEP-7. In the glassy state, the storage moduli of the PETG−SEP nanocomposites are higher than that of pure PETG, indicating that well-dispersed mixed structures with good interfacial PETG−SEP bonding enhance the mechanical properties of the composites.

3.2. Mechanical Properties of 3D Printed Samples.

The mechanical properties of the injection-molded and 3D-printed polymer composites were measured in the direction parallel to deposition (vertical samples) and in the direction perpendicular to deposition (horizontal samples), as shown in Figure 2.

The experimental results of the injection-molded samples show that the tensile strengths and elastic modulus are improved with increasing SEP concentration. At the SEP concentration of 5 phr, the tensile strength is increased to 51.5 from 43.2 MPa (control, pure PETG), while the elastic modulus is increased to 272.9 from 253.4 MPa (control, pure PETG). Simultaneously, the elongation at break of the different samples is decreased with an increases in SEP loading, as shown in Figure S5. This phenomenon is explained by the higher physical strengths of the PETG−SEP nanocomposites relative to that of pure PETG, which arise because the modulus and strength of SEP are higher than those of PETG. Moreover, the well-dispersed nanoscale additives restrict the mobility of the polymer matrix molecular chains, yielding higher stiffness and lower elongation of the nanocomposites. Similar tendencies and experimental results have been reported previously.[2,10,18,25,27−29]

The tensile strengths and elastic moduli of specimens prepared by 3D printing in the vertical and horizontal directions are shown in Figure 2. For the vertical-direction samples, the SEP-3 FDM 3D-printed samples show a tensile strength increased to 51.0 from 37.7 MPa (control, pure PETG); the elastic modulus is increased to 252.9 from 197.81 MPa (control, pure PETG). For the horizontal-direction samples, the SEP-2 FDM 3D printed samples show a tensile strength increased to 33.1 from 15.4 MPa (control, pure PETG); the elastic modulus is increased to 229.0 from 168.6 MPa (control, pure PETG).

The pure PETG prepared by injection molding shows a higher tensile strength than the FDM 3D-printed PETG. This may arise from several phenomena. First, during the FDM 3D printing process, the molten filament is attached to the surface of a solid layer, yielding poor entanglement of the polymer molecule.[2,15,22−24] Second, as shown in Figure 2a, printed filaments in the FDM process are inevitably separated by gaps,[6,29] causing voids in the printed objects that reduce the mechanical properties of the printed material. Third, as the printer head passes over the previously deposited material, deformation of the sample deposit occurs because of the heat of the printer head, thus causing stress concentration and the deterioration of properties in the deformed portion.[3] For these reasons, the physical properties of the 3D-printed samples using pure PETG are poor compared to those of the injection-molded samples. However, when SEP is composited with PETG, the rate of increase in the physical properties of the 3D-

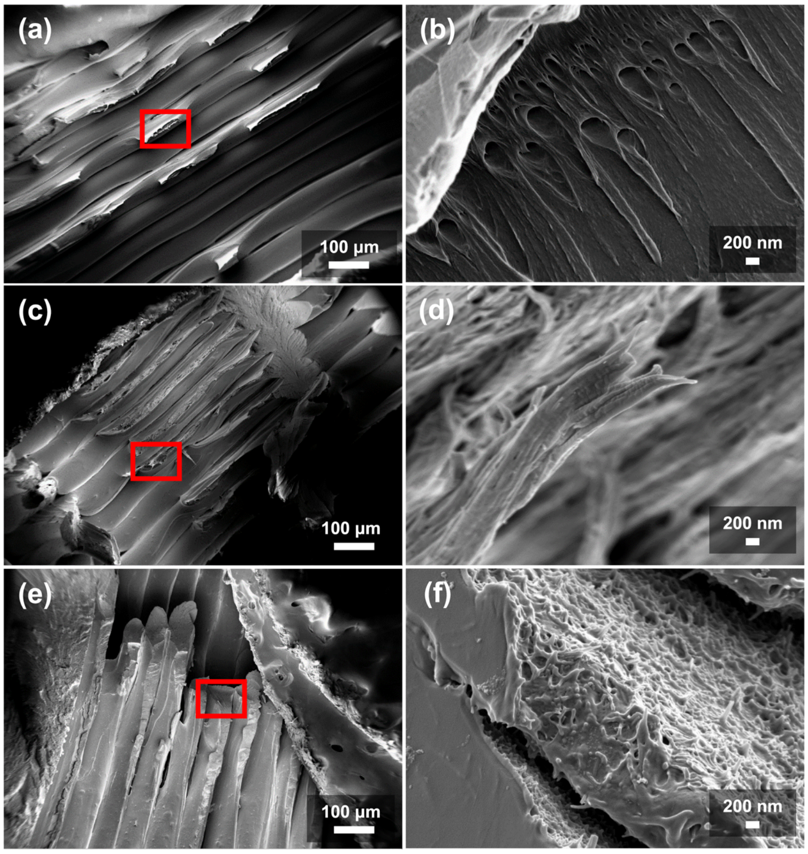

Figure 5. SEM image of post-tensile fracture surface observation of 3D printed PETG composites with tension applied in horizontal direction. (a,b) Pure PETG, (c,d) SEP-3 composite, (e,f) SEP-7 composite.

printed samples exceeds that observed in the injection-molded samples with increasing SEP contents. The study is conducted to understand this synergistic effect on the reinforcement of mechanical properties for PETG−SEP formed via 3D printing.

3.3. Morphological Properties of PETG−SEP Composites. The morphology of pure SEP before dispersion in PETG resin is observed through SEM. As shown in Figure 3, needle-shaped SEP particles are bundled and show no overall orientation. These SEM results are reported for comparison with the PETG−SEP composites.

The tensile fracture surfaces of the injection-molded specimens are observed. The pure PETG is stretched, as shown in Figure 4a,b. In the high-magnification image, the polymer resin shows a very clean fracture surface. Figure 4c,d shows the injection-molded SEP-3 tensile fracture surface. The photographs show a weak fibrous texture in the polymer, and the heads and bodies of the SEP bundles are also observed. The irregular orientation of the SEP bundles can be inferred from the irregular distributions of the heads and bodies shown in the photographs of Figure 4e,f.

The tensile fracture surfaces of the specimens printed in the horizontal direction (transverse direction relative to the print path) are observed. The polymer without SEP is stretched, as shown in Figure 5a,b. As the observation magnification of SEM increases, the surface of the deformed part of the polymer is confirmed to remain clean. However, the deformation behavior of the polymer changes with the inclusion of different concentrations of SEP. Figure 5c,d shows the fracture surface of SEP-3, which demonstrates a fractured and fibrous texture. This texture is not observed for pure PETG. It is presumed that the interfacial interaction between SEP and PETG is favorable and that the deformation pattern is changed by this fibrous feature. As the content of SEP increases, the features of the fracture surface also change. The surface of the SEP-7 sample is visible in Figure 5f; it shows increased roughness, but on fibrous texture, it is visible, unlike the surface of SEP-3. The fibrous texturing of the material occurs because the nanoclay dispersed inside the printed body resists the deformation of the PETG matrix. However, the SEP-7 sample shows a different fracture surface than the SEP-3 sample because as the SEP concentration exceeds the optimum nanoclay content of 3 phr, the interfacial breakdown of the material occurs before the maximum resistance to deformation can be reached. In the tensile fracture of the 3D-printed sample with tension applied in the direction parallel to printing, it is possible to deduce that the fracture proceeds by traversing the printed filament in the direction perpendicular to the direction of orientation of the SEP needle-like particles. The fracture surface morphology enables the indirect deduction of the orientation and reinforcement effect of the SEP nanoparticles. The fractured section of the tensile sample printed in the vertical direction of pure PETG is depicted in Figure 6. As shown in Figure 6a, the space between the filaments is increased, and the deformed fracture surface of the polymer is smooth, as shown in Figure 6b. The tensile fracture surface of the vertically printed SEP-3 sample shows enlarged voids from the deformation of the material, as confirmed by Figure 6c. The surface roughness of SEP-3 is increased, as shown in Figure 6d, at higher magnification. Figure 6d also shows the estimated part of the SEP particle head with an oriented surface. The fracture profile

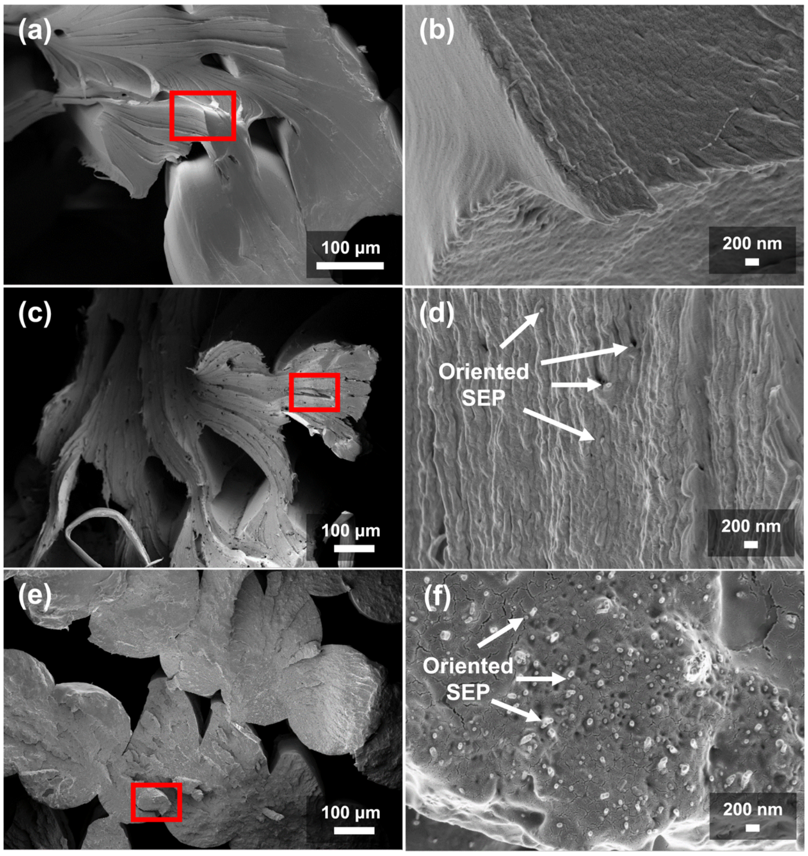

Figure 6. SEM image of post-tensile test fracture surface observation of 3D printed PETG with tension applied in vertical direction. (a,b) Pure PETG, (c,d) SEP-3 composite, (e,f) SEP-7 composite.

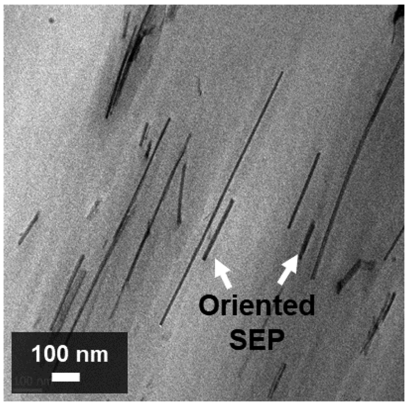

Figure 7. TEM image of oriented SEP particles in 3D printed SEP-3 composite.

of the SEP-7 sample observed by SEM (Figure 6e) also shows a small amount of pore changes in the fracture surface because of its low strain at fracture. The roughness of the fracture surface is increased, and irregular shapes are observed. The body part and the missing parts of the SEP fibers are simultaneously identified in Figure 6f.

It can be concluded through SEM observation that SEP affects the deformation and fracture behavior of the overall material in composites with PETG, and it can be deduced that this behavior is related to the change of the tensile strength characteristics of the composite. However, it is not sufficient to discuss the orientation of SEP within PETG based only on the SEP particles exposed on the samples' fracture surfaces. Therefore, structural observation using TEM is performed to confirm the structures of SEP within the composite materials.

The distributions of SEP and the nanocomposite morphologies were observed by TEM. Representative TEM micrographs of SEP-3 are shown in Figure 7. These images include dark lines that represent the plates of aligned SEP; these are distributed in the PETG polymer matrix in the same direction, forming a well-dispersed and oriented structure in the nanocomposites. At 3 phr SEP, the PETG matrix shows high mechanical strength with SEP and produces a good dispersion. The result is the same as the X-ray diffraction result in which SEP demonstrates a certain orientation. In this experiment, we observed more than 50 particles in the sample, all showing the same orientation. This is attributed to the reorientation of SEP during the filament extrusion and winding process and the repeated reorientation during the extrusion process of 3D printing through the 400 μm nozzle. However, because TEM is limited to localized observation sites, we performed SAXS experiments to understand the role of the filler material and the degree of orientation over larger areas of the composites.

3.4. Anisotropic Structure of SEP in the PETG. SAXS was performed to confirm the orientation structure of SEP in the PETG over a large area. First, the internal structures of injection-molded PETG specimens containing SEP in the same concentrations as SEP-3 and SEP-5 are characterized using SAXS. A collimated X-ray beam penetrated the sample and the scattered X-ray beam was collected using a 2D detector. As shown in Figure 8, scattering patterns of symmetrical circular shapes are obtained from the injection-molded samples; these

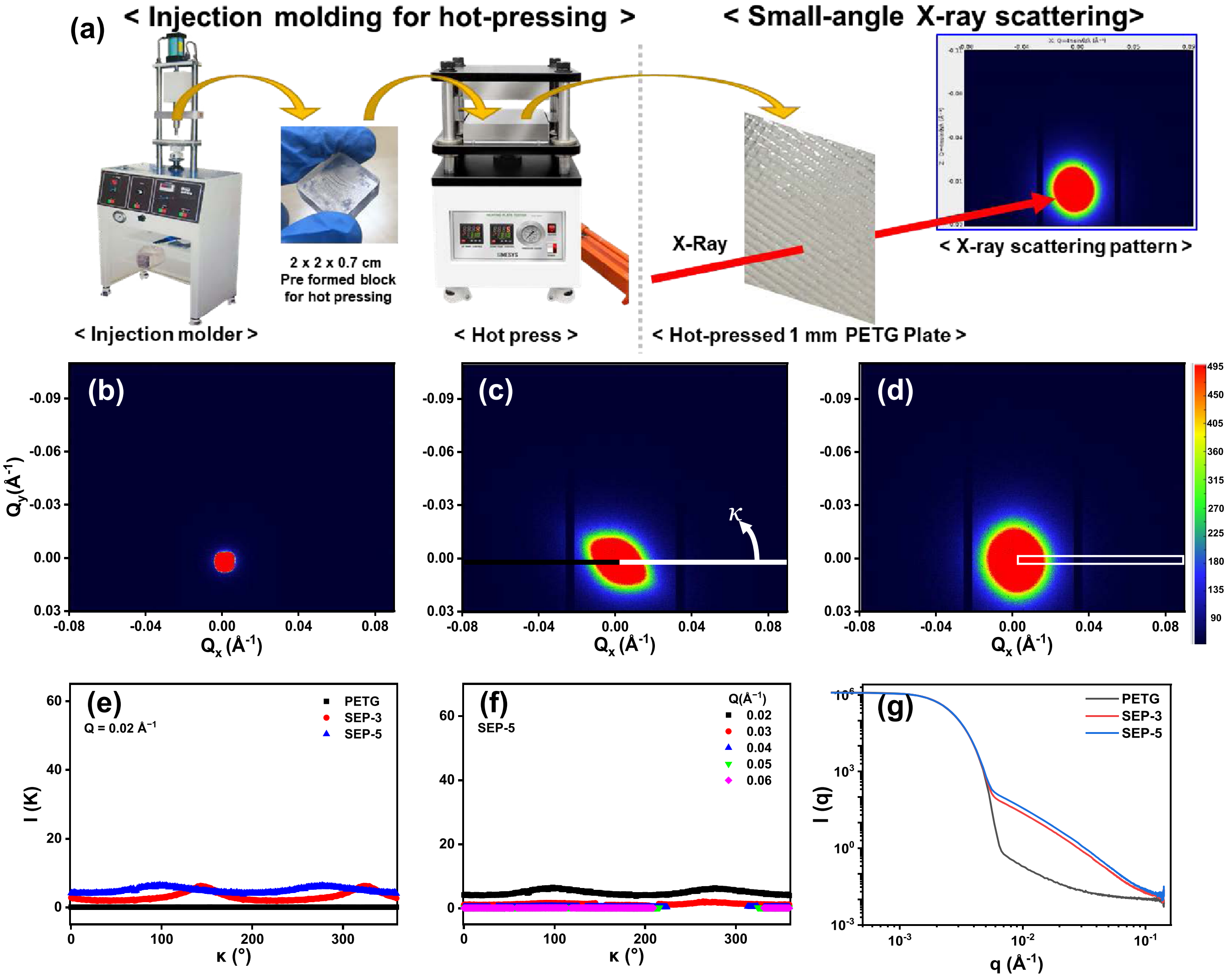

Figure 8. Sample preparation method and experimental results for SAXS measurement. (a) Schematic of injection molding and hot-pressing process for SAXS measurement. SAXS data from hot-pressed sheets of (b) pure PETG, (c) SEP-3 composite, and (d) SEP-5 composite. (e) Azimuthal scattering intensity as a function of SEP concentration in composite at $q = 0.02$ Å^{-1}. (f) Azimuthal scattering intensity as a function of Q-values in the SEP-5 composite. (g) Integration of the region bounded by the white rectangle along Q_y yields the scattering profiles as a function of Q_x for hot-pressed sheets of PETG, SEP-3, and SEP-5.

imply the isotropic orientation of the SEP particles in the composites.

The 3D printed samples were mounted with the printing direction perpendicular to the sample stage. Figure 9b−d depicts 2D contour plots of the scattering from the pure PETG, SEP-3, and SEP-5 samples. The results show that the 2D scattering data exhibit anisotropic elliptical patterns, rather than the isotropic circles observed in Figure 8, for SEP-3 and SEP-5. The direction of the major axis of the ellipse is perpendicular to the printing direction. Figure 9e,f shows azimuthal scattering as functions of the magnitude of the scattering vector $Q = \sqrt{(Q_x^2 + Q_y^2 + Q_z^2)}$ at different SEP concentrations, that is, the scattering intensity versus the angle of scattering. The SEP concentration-dependent azimuthal scattering intensities are measured for a selected $q = 0.02$ Å^{-1}, as shown in Figure 9e, where the anisotropy of the scattering pattern is more clearly visible. From Figure 9e, peaks with two symmetric intensities are obtained, which coincide with the 2D contour data of anisotropic scattering. These symmetrical peaks are maintained at Q_x reaching 0.04 Å^{-1}; beyond this point, minimal scattering intensity is obtained (Figure 9f). The intensity remains constant for SEP-3 and SEP-5. The 3D-printed samples of pure PETG shows no such features (Figure 9e).Thus, considering the results shown in Figures 8 and 9, the anisotropic scattering shown by 3D-printed PETG−SEP composites can be interpreted as arising from the orientation of the SEP particles, which is only initiated by the 3D printing process.

Therefore, we conclude from these SAXS results that the scattering features originate from the SEP particles in PETG and their arrangement parallel to the 3D printing direction. In addition, because no specific reflection peak occurs in the scattering profiles (Figure 9e,g), we can conclude that the spacings of the oriented SEP rods are not regular in the PETG matrices.

Figure S6 illustrates the improvement of the orientation of the SEP of the stretched SEP-3 and SEP-5 tensile samples. For both SEP-3 and SEP-5, the scattering patterns were anisotropically elongated, with the greatest change observed in the direction perpendicular to the stretched direction (refer to 2D

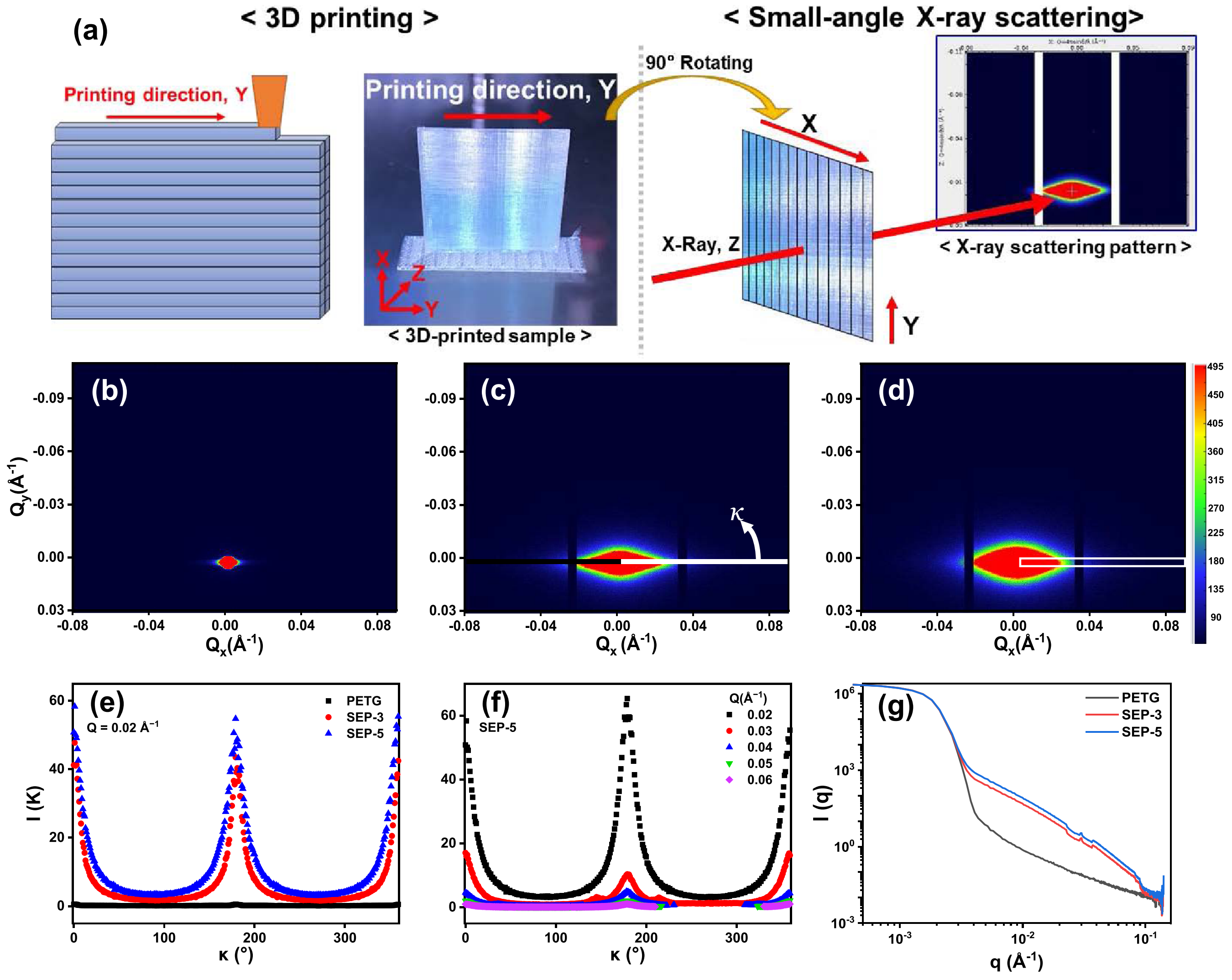

Figure 9. Sample preparation method and experimental results for SAXS measurement. (a) Schematic of 3D printing, rotation, and SAXS measurement. SAXS data from 3D printed sheets of (b) pure PETG, (c) SEP-3 composite, and (d) SEP-5 composite. (e) Azimuthal scattering intensity as a function of SEP concentration in composite at $q = 0.02$ Å^{-1}. (f) Azimuthal scattering intensity as a function of Q-values in the SEP-5 composite. (g) Integration of the region bounded by the white rectangle along Q_y yields the scattering profiles as a function of Q_x for 3D-printed sheets of PETG, SEP-3, and SEP-5.

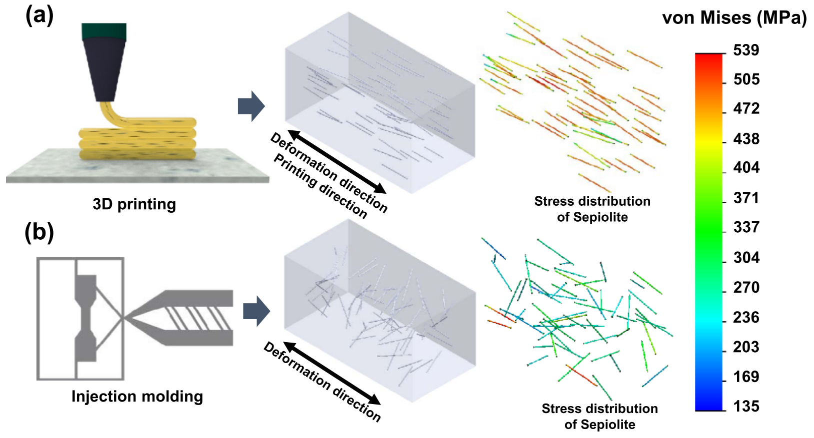

Figure 10. According to the fabrication methods of (a) 3D printing vs (b) injection molding of PETG−SEP nanocomposite, SEP structures are formed in the composite, and the effects of the von Mises stress applied to SEP according to the structure are visualized through simulation.

scattering data shown in Figure S6b,c). The improvement in orientation was also evident in the results of azimuthal scattering intensities plotted at $q = 0.04$ Å^{-1}, where the 3D-printed samples showed higher peaks after undergoing the tensile test (Figure S6d,e). This clearly indicates that the orientations of the 3D-printed SEP-3 and SEP-5 were improved by stretching. Considering the comprehensive results of this study, the physical and chemical interaction models of the material are as suggested in Figures S4 and 10. In Figure S3, the rheological and viscoelastic behaviors of SEP and PETG are explained by the chemical interaction of the materials. The simulation model in Figure 10 shows that when the direction of PETG matrix deformation coincides with the SEP orientation direction, excellent mechanical tensile property reinforcement occurs.

3.5. Simulation of the Reinforcement Effect of SEP in PETG. The results in Figures 10 and S4 show that a deformation of about 0.95 μm in length occurs for a sample with SEP under a tensile force of 0.01 N; with randomly oriented SEP, the deformation is approximately 1.05 μm. The SEP stress is 537 MPa in the length-oriented composite and 539 MPa in the randomly oriented composite. Therefore, the stiffness of the composite in which SEP is present with length-direction orientation is increased compared to the composite with a random dispersion. The stiffness indicates the degree of resistance to deformation in response to the force applied to an object.

In other words, the smaller strain under the same tensile force shown by a composite containing equal concentrations of SEP indicates that the resistance to deformation by SEP is increased when SEP is oriented lengthwise relative to the tensile direction.

The lengthwise-oriented SEP is subject to a higher overall stress, which means that it is more resistant to tensile deformation than the relatively randomized SEP; therefore, the composite with oriented SEP shows increased stiffness.

4. CONCLUSIONS

In this study, we demonstrated the fabrication of PETG−SEP nanocomposites by the 3D printing of extruded PETG−SEP filaments. The good dispersion and mechanical reinforcement effects provided by the highly oriented nanoclay fiber particles in the 3D printed filament were tested and confirmed. By comparing the tensile strengths of injection-molded and 3D printed samples, it was confirmed that the PETG−SEP nanocomposites formed by FDM 3D printing showed greater reinforcement of the physical properties than of the material formed by injection molding. The tensile fracture surfaces were observed with SEM. The fibrous texture of the material was confirmed by the appearance of the fracture surfaces, and an SEP particle directional alignment parallel to the deposition direction was identified. In the SEP-3 sample, breakage of the middle portion of the SEP fiber was observed. The orientations and structure of the SEP dispersed in the PETG matrix were observed using TEM, which showed that the highly oriented SEP was uniformly distributed within the matrix. Although the degrees of dispersion and orientation of SEP in small regions were confirmed by SEM and TEM, it was difficult to confirm the overall structure of the composites. Therefore, SAXS was used to determine the overall structure and dispersion; the results confirmed the SEM and TEM observations over larger area of composites. In order to confirm the physical and rheological interactions of PETG and SEP, the degrees of interaction between SEP and PETG were verified by viscoelasticity and viscosity measurements. For the PETG−SEP composite filament passing through the nozzle of the 3D printer, thinning behavior was expected, and excellent material compatibility was confirmed. With the identification of the behaviors of SEP in the 3D printing environment, we expect this work to become a foundation for the application of nanomaterials such as nanoclay, CNTs, and CNC in FDM 3D printing. Specifically, the application of oriented PETG−SEP in FDM 3D printings seems to overcome the physical limitations of existing 3D printing materials.

■ ASSOCIATED CONTENT

Supporting Information

The Supporting Information is available free of charge at https://pubs.acs.org/doi/10.1021/acsami.0c03830.

> TEM images of oriented sepiolite structures, schematic of PETG−SEP nanocomposites, schematic of the chemical bonding forces, 3D printing and injection molding, mechanical property measurements, and sample preparation method and experimental results for SAXS measurement (PDF)

■ AUTHOR INFORMATION

Corresponding Author

Hyun-Joong Kim − *Laboratory of Adhesion & Bio-Composites, Program in Environmental Materials Science and Research Institute of Agriculture and Life Sciences, College of Agriculture & Life Sciences, Seoul National University, Seoul 08826, Republic of Korea*; orcid.org/0000-0002-4447-4553; Email: hjokim@snu.ac.kr; Fax: +82 28732318

Authors

Hoon Kim − *Laboratory of Adhesion & Bio-Composites, Program in Environmental Materials Science, Seoul National University, Seoul 08826, Republic of Korea*

Kwang-Hyun Ryu − *Laboratory of Adhesion & Bio-Composites, Program in Environmental Materials Science, Seoul National University, Seoul 08826, Republic of Korea*

Dooyoung Baek − *Laboratory of Adhesion & Bio-Composites, Program in Environmental Materials Science, Seoul National University, Seoul 08826, Republic of Korea*; orcid.org/0000-0001-7727-8770

Tanveer Ahmed Khan − *Laboratory of Adhesion & Bio-Composites, Program in Environmental Materials Science, Seoul National University, Seoul 08826, Republic of Korea*

Sungchul Shin − *Department of Biosystems and Biomaterials Science and Engineering, Seoul National University, Seoul 08826, Republic of Korea*

Jinho Hyun − *Department of Biosystems and Biomaterials Science and Engineering and Research Institute of Agriculture and Life Sciences, College of Agriculture & Life Sciences, Seoul National University, Seoul 08826, Republic of Korea*; orcid.org/0000-0002-9992-5681

Jin Soo Ahn − *Dental Research Institute and Department of Orthodontics, School of Dentistry, Seoul National University, Seoul 08826, Republic of Korea*

Sug-Joon Ahn − *Dental Research Institute and Department of Orthodontics, School of Dentistry, Seoul National University, Seoul 08826, Republic of Korea*

Hyun Jeong Kim − *Dental Research Institute and Department of Orthodontics, School of Dentistry, Seoul National University, Seoul 08826, Republic of Korea*

Jaseung Koo − *Department of Organic Materials Engineering, Chungnam National University, Daejeon 34134, Republic of Korea*; orcid.org/0000-0002-3646-0805

Complete contact information is available at:
https://pubs.acs.org/10.1021/acsami.0c03830

Notes

The authors declare no competing financial interest.

■ ACKNOWLEDGMENTS

This work was supported by Seoul National University Research Grant in 2018. Experiments were carried out through free support of Anton Paar Korea's rheometer test equipment, and we would like to thank to Anton Paar Korea and HyunJoo Lee and SeolHee Jeon of Anton Paar Korea and Yu-Kyung Oh of National Instrumentation Center for Environmental Management and JongHwa Cho and JungWoo Ko of Technical Team of KNsolution for helping us.

■ REFERENCES

(1) Jones, N. Science in Three Dimensions: the Print Revolution. *Nature* **2012**, *487*, 22−23.

(2) Gnanasekaran, K.; Heijmans, T.; Van Bennekom, S.; Woldhuis, H.; Wijnia, S.; de With, G.; Friedrich, H. 3D printing of CNT- and graphene-based conductive polymer nanocomposites by fused deposition modeling. *Appl. Mater. Today* **2017**, *9*, 21−28.

(3) Weng, Z.; Wang, J.; Senthil, T.; Wu, L. Mechanical and thermal properties of ABS/Montmorillonite Nanocomposites for Fused Deposition Modeling 3D printing. *Mater. Des.* **2016**, *102*, 276−283.

(4) Le Duigou, A.; Barbé, A.; Guillou, E.; Castro, M. 3D Printing of Continuous Flax Fibre Reinforced Biocomposites for Structural Applications. *Mater. Des.* **2019**, *180*, 107884.

(5) Tian, X.; Liu, T.; Yang, C.; Wang, Q.; Li, D. Interface and performance of 3D printed continuous carbon fiber reinforced PLA composites. *Composites, Part A* **2016**, *88*, 198−205.

(6) Blok, L. G.; Longana, M. L.; Yu, H.; Woods, B. K. S. An Investigation into 3D Printing of Fibre Reinforced Thermoplastic Composites. *Addit. Manuf.* **2018**, *22*, 176−186.

(7) Szykiedans, K.; Credo, W.; Osiński, D. Selected Mechanical Properties of PETG 3-D prints. *Procedia Eng.* **2017**, *177*, 455−461.

(8) Wojtyła, S.; Klama, P.; Baran, T. Is 3D printing Safe? Analysis of the Thermal Treatment of Thermoplastics: ABS, PLA, PET, and Nylon. *J. Occup. Environ. Hyg.* **2017**, *14*, D80−D85.

(9) Christ, J. F.; Aliheidari, N.; Ameli, A.; Pötschke, P. 3D Printed Highly Elastic Strain Sensors of Multiwalled Carbon Nanotube/Thermoplastic Polyurethane Nanocomposites. *Mater. Des.* **2017**, *131*, 394−401.

(10) Chen, Q.; Mangadlao, J. D.; Wallat, J.; De Leon, A.; Pokorski, J. K.; Advincula, R. C. 3D Printing Biocompatible Polyurethane/Poly(lactic acid)/Graphene Oxide Nanocomposites: Anisotropic Properties. *ACS Appl. Mater. Interfaces* **2017**, *9*, 4015−4023.

(11) Melenka, G. W.; Cheung, B. K. O.; Schofield, J. S.; Dawson, M. R.; Carey, J. P. Evaluation and Prediction of the Tensile Properties of Continuous Fiber-reinforced 3D Printed Structures. *Compos. Struct.* **2016**, *153*, 866−875.

(12) Dupaix, R. B.; Boyce, M. C. Finite strain behavior of poly(ethylene terephthalate) (PET) and poly(ethylene terephthalate)-glycol (PETG). *Polymer* **2005**, *46*, 4827−4838.

(13) Franciszczak, P.; Piesowicz, E.; Kalniņš, K. Manufacturing and properties of r-PETG/PET fibre composite - Novel approach for recycling of PETG plastic scrap into engineering compound for injection moulding. *Composites, Part B* **2018**, *154*, 430−438.

(14) Dawoud, M.; Taha, I.; Ebeid, S. J. Mechanical Behaviour of ABS: An Experimental Study using FDM and Injection Moulding Techniques. *J. Manuf. Process.* **2016**, *21*, 39−45.

(15) Kang, T. H.; Compton, B. G.; Heller, W. T.; Qian, S.; Smith, G. S.; Urban, V. S.; Duty, C. E.; Do, C. Potentials with small-angle neutron scattering technique for understanding structure-property relation of 3D-printed materials. *Polym. Eng. Sci.* **2019**, *59*, E65−E70.

(16) Kim, H.; Park, J.-W.; Kim, H.-J. Flame Retardant Nano-Composites Containing Nanofillers. *Science and Applications of Tailored Nanostructures*; One Central Press, 2017; pp 2−24.

(17) del Rio, M. S.; Garcia-Romero, E.; Suarez, M.; da Silva, I.; Fuentes-Montero, L.; Martinez-Criado, G. Variability in Sepiolite: Diffraction Studies. *Am. Mineral.* **2011**, *96*, 1443−1454.

(18) Tabatabaei-Yazdi, Z.; Mehdipour-Ataei, S. Poly(ether-imide) and related sepiolite nanocomposites: investigation of physical, thermal, and mechanical properties. *Polym. Adv. Technol.* **2015**, *26*, 308−314.

(19) Kim, H.; Park, J.-W.; Lee, J.-H.; Jang, S.-W.; Kim, H.-J.; Choi, Y.; Choy, J.-H.; Yang, J.-H. Clay-organic Intumescent Hybrid System for the Synergetic Flammability of Polymer Nanocomposites. *J. Therm. Anal. Calorim.* **2018**, *132*, 2009−2014.

(20) Carneiro, O. S.; Silva, A. F.; Gomes, R. Fused Deposition Modeling with Polypropylene. *Mater. Des.* **2015**, *83*, 768−776.

(21) Zhang, J.; Wang, X. Z.; Yu, W. W.; Deng, Y. H. Numerical Investigation of the Influence of Process Conditions on the Temperature Variation in Fused Deposition Modeling. *Mater. Des.* **2017**, *130*, 59−68.

(22) Yin, J.; Lu, C.; Fu, J.; Huang, Y.; Zheng, Y. Interfacial Bonding During Multi-Material Fused Deposition Modeling (FDM) Process due to Inter-molecular Diffusion. *Mater. Des.* **2018**, *150*, 104−112.

(23) Abbott, A. C.; Tandon, G. P.; Bradford, R. L.; Koerner, H.; Baur, J. W. Process-structure-property Effects on ABS Bond Strength in Fused Filament Fabrication. *Addit. Manuf.* **2018**, *19*, 29−38.

(24) Raney, J. R.; Compton, B. G.; Mueller, J.; Ober, T. J.; Shea, K.; Lewis, J. A. Rotational 3D Printing of Damage-tolerant Composites with Programmable Mechanics. *Proc. Natl. Acad. Sci. U.S.A.* **2018**, *115*, 1198−1203.

(25) Siqueira, G.; Kokkinis, D.; Libanori, R.; Hausmann, M. K.; Gladman, A. S.; Neels, A.; Tingaut, P.; Zimmermann, T.; Lewis, J. A.; Studart, A. R. Cellulose Nanocrystal Inks for 3D Printing of Textured Cellular Architectures. *Adv. Funct. Mater.* **2017**, *27*, 1604619.

(26) Jim, C. Y. Impregnation of Moist and Dry Unconsolidated Clay Samples using Spurr Resin for Microstructural Studies. *J. Sediment. Res.* **1985**, *55*, 597−599.

(27) Shim, S. H.; Kim, K. T.; Lee, J. U.; Jo, W. H. Facile Method to Functionalize Graphene Oxide and Its Application to Poly(ethylene terephthalate)/Graphene Composite. *ACS Appl. Mater. Interfaces* **2012**, *4*, 4184−4191.

(28) Liu, Y.; Kumar, S. Polymer/Carbon Nanotube Nano Composite Fibers-A Review. *ACS Appl. Mater. Interfaces* **2014**, *6*, 6069−6087.

(29) Tekinalp, H. L.; Kunc, V.; Velez-Garcia, G. M.; Duty, C. E.; Love, L. J.; Naskar, A. K.; Blue, C. A.; Ozcan, S. Highly oriented carbon fiber-polymer composites via additive manufacturing. *Compos. Sci. Technol.* **2014**, *105*, 144−150.

(30) Carreau, P.; De Kee, D.; Chhabra, R. *Rheology of Polymeric Systems: Principles and Applications*; Hanser: New York, 1997.

(31) Bagheriasl, D.; Carreau, P. J.; Riedl, B.; Dubois, C.; Hamad, W. Y. Shear rheology of polylactide (PLA)-cellulose nanocrystal (CNC) nanocomposites. *Cellulose* **2016**, *23*, 1885−1897.

(32) Khoshkava, V.; Kamal, M. R. Effect of Cellulose Nanocrystals (CNC) Particle Morphology on Dispersion and Rheological and Mechanical Properties of Polypropylene/CNC Nanocomposites. *ACS Appl. Mater. Interfaces* **2014**, *6*, 8146−8157.

(33) Abbasi, S.; Carreau, P. J.; Derdouri, A.; Moan, M. Rheological Properties and Percolation in Suspensions of Multiwalled Carbon Nanotubes in Polycarbonate. *Rheol. Acta* **2009**, *48*, 943.

(34) Ray, S. S.; Yamada, K.; Okamoto, M.; Ueda, K. New Polylactide-layered Silicate Nanocomposites. 2. Concurrent Improvements of Material Properties, Biodegradability and Melt Rheology. *Polymer* **2003**, *44*, 857−866.

(35) Du, F.; Scogna, R. C.; Zhou, W.; Brand, S.; Fischer, J. E.; Winey, K. I. Nanotube Networks in Polymer Nanocomposites: Rheology and Electrical Conductivity. *Macromolecules* **2004**, *37*, 9048−9055.